

# Impacts of Nuclear-Reactor-Physics Models for Secondary Photons on Coupled Photon-Electron-Positron Transport Problems


Ahmed Naceur,<sup>1,\*</sup> Gabriel Famulari<sup>2,3,†</sup>, Charles Bienvenue<sup>1,‡</sup>, Jean-François Carrier,<sup>2,3,§</sup> and Alain Hébert<sup>4,¶</sup>

<sup>1</sup>Department of Engineering Physics, Nuclear Engineering Institute, École Polytechnique de Montréal, Québec H3T 1J4, Canada

<sup>2</sup>CRCHUM, Centre hospitalier de l'Université de Montréal, Québec H2L 4M1, Canada

<sup>3</sup>Physics Department, Université de Montréal, Québec H3C 3J7, Canada

<sup>4</sup>Department of Mechanical Engineering, Nuclear Engineering Institute, École Polytechnique de Montréal, Québec H3T 1J4, Canada

 (Received 22 November 2021; revised 7 May 2022; accepted 23 August 2022; published 4 November 2022)

Fully coupled photon-electron-positron computational schemes are needed in a broad range of domains, from radiotherapy and radiosurgery treatment planning to nuclear-reactor safety analysis. Industrial deployment of such schemes remains problematic because of the prohibitively time-consuming charged-particle-transport aspects of both Monte Carlo algorithms and Boltzmann-Fokker-Planck solvers. In this paper, a partially coupled scheme based on reactor-physics models for secondary photons (RPSPs) is presented. RPSPs include thick-target-bremsstrahlung, annihilation, and full atomic cascade models, recovering long-range effects of both electrons and positrons. The RPSP-based scheme is compared with state-of-the-art fully coupled and uncoupled schemes in medical, nuclear, and multidisciplinary contexts. Within tissues, the average discrepancies from the fully coupled scheme are about 0.5%, with a maximum error below 1.3% at high energy. The CPU time of the coupled schemes is reduced by 58 and 78 times for 3- and 6-MeV beams, respectively. The discrepancies are also within the accuracy of the cross sections for  ${}^4\text{Be}$ ,  ${}^6\text{C}$ ,  ${}^{13}\text{Al}$ ,  ${}^{26}\text{Fe}$ ,  ${}^{29}\text{Cu}$ ,  ${}^{32}\text{Ge}$ ,  ${}^{47}\text{Ag}$ ,  ${}^{79}\text{Au}$ ,  ${}^{82}\text{Pb}$ , and  ${}^{92}\text{U}$  slabs. The same discrepancies are about 0.1%, 0.4% and 0.8%, respectively, in the reactor's shielding, vessel and fuel slabs. A power peaking factor reduction of 4.35 times from the state-of-the-art uncoupled scheme is demonstrated for uranium oxide and mixed plutonium-uranium oxide slabs.

DOI: [10.1103/PhysRevApplied.18.054015](https://doi.org/10.1103/PhysRevApplied.18.054015)

## I. INTRODUCTION

Following Hubbell's radiation-physics definition [1], Garth's [100 eV, 30 MeV] encyclopedic survey [2] concluded with a list of 36 separate and compartmentalized disciplines, where the quantities of interest can be obtained only by means of a coupled nonplasma photon-electron-positron transport calculation. When it comes to the development and deployment of computational-physics infrastructure, it appears that the nuclear [3,4], medical [5–7], and space [8–10] sectors have financed major work leading to deterministic Boltzmann solvers and Monte Carlo (MC) codes.

(a) *Space interest.* Beyond low Earth orbit, it has been established, for both intravehicular and extravehicular activities, that (1) astronauts must be protected against galactic cosmic rays and solar-particle events and (2) the degree of damage inflicted on equipment needs to be quantified and monitored [11]. The trapped electrons in the Van Allen Belts, because of their abundance, spatial distribution, and energies, form the primary source within the structure. They deliver the total integrated dose, and initiate and accelerate displacement cascades, interstitials, and dislocations [12,13].

(b) *Nuclear interest.* In fission nuclear reactors, photons are produced during prompt and delayed fission, inelastic neutron scattering, radioactive decay, radioactive capture, restructuring cascades, and charged-particle ( $\beta^\mp$ ,  $e^\mp$ ) thermalization. Although the photon and electron fluxes are approximately 3 and 6 times higher, respectively, than that of neutrons [14–16], current reactor computational chains consider only neutron transport. Such a hypothesis is generally supported by six arguments: (1) only

\*ahmed.naceur@polymtl.ca

†gabriel.famulari.chum@ssss.gouv.qc.ca

‡charles.bienvenue@polymtl.ca

§jean-francois.carrier.2@umontreal.ca

¶alain.hebert@polymtl.ca

neutrons govern and temper the core's criticality [17], (2) the fallout of the assumption is ultraconservative from an operational-safety perspective [18], (3) the current neutronic complexity to handle the resonant self-shielding aspects [19], (4) the time-consuming aspects of such a coupling problem [20], (5) the current priority of a thermomechanical-neutronic (multiphysics) coupling [21] and (6) the state-of-the-art theory limitation aspects for deterministic or MC charged particle transport [22–24]. Imposing local energy deposition for both photons and electrons therefore overestimate the power peaking factor (PPF). The latter defines the local power density and the departure from the nucleate boiling ratio, which together form the two pillars of the core-protection calculator system and the core-operation limit supervisory system [25]. Liegeard *et al.* [26] showed that coupling primary photons implies immediate PPF reductions of more than 1% for uranium oxide (UOX) and mixed plutonium-uranium oxide (MOX) in pressurized-water-reactor (PWR) assemblies, and 30% for burnable-gadolinium PWR assemblies. The economic contribution reported by Liegeard neglects consideration of electron transport and any secondary photons (bremsstrahlung, annihilation, and fluorescence). These observations emphasize the ambitions of plant operators for better evaluation of the PPF, aimed at possible ramp-up [27].

(c) *Medical interest.* The main goal of radiotherapy treatment planning is to give a sufficient dose to the target to achieve local tumor control while limiting the risk of normal-tissue complications in surrounding organs at risk. It is only in this case that an optimal curative effect can be expected [28]. The success of such a treatment plan depends on the accuracy of the coupled dose-distribution calculation within the patient's anatomy [29]. On the other hand, treatment planning is inherently associated with multiple sources of uncertainty (gross-tumor-volume delineation errors, unknown microtumor extension beyond the gross tumor volume, patient organ-anatomy variation, and setup fluctuations) [30]. Therefore, the International Commission on Radiation Units and Measurements recommends a maximum of 5% accumulated error between treatment planning and delivery [31]. The 5% threshold is recognized as a severe change in tissue response [32]. Execution errors are subject to clinical conditions, involve random and systematic components, and are difficult to quantify, prevent, and detect [33]. The American Association of Physicists in Medicine (AAPM) recommends that planning errors should be in the range of 2% or 2 mm (absolute distance from agreement) or less so that the accuracy of the total dose delivered does not exceed the goal of 3% or 3 mm [34]. The intrinsically time-consuming nature of MC simulations has driven medical physicists to completely abandon formal particle transport in clinical routine in favor of semiempirical models. Point-kernel models [35], pencil-beam models [36–38], collapsed-cone

convolution [39], and convolution and superposition [40,41] are the main clinical models deployed, all derived from Hogstrom *et al.*'s adaptation [42] of the Fermi-Eyges small-angle scattering theory [43,44]. The major limits of these models arise from their assumptions: (1) a pre-established dose distribution in a homogeneous phantom is needed for the convolution, (2) the patient's anatomy is approximated by a homogeneous infinite medium, (3) an electronic equilibrium is assumed everywhere, (4) interface effects are neglected, and (5) attenuation effects are considered only on the beam axis. Several correction factors have been proposed to remedy these limits: the partial heterogeneity corrections of Ahnesjö *et al.* (for photon beams) [38] and Knoos *et al.* (for electron beams) [45], the lateral scaling of Ulmer *et al.* [46], and the buildup models of Tillikainen *et al.* [47]. The improvement remains partial and unsatisfactory for strong heterogeneities and narrow beams. Typical dosimetric errors can reach 22% following a density increase in homogeneous tissue [48], and 40% in the presence of heterogeneities [49]. Model-based dose-calculation algorithms are starting to emerge in clinical routine, targeting the reduction of such errors [50].

The inordinate computational effort of the coupled transport problem arises from the highly irregular nature of electron-matter interactions. Berger and Wang [51] showed that electrons and positrons scatter 3000 and 4000 times more than neutrons and photons when they slow down by 250 keV in aluminum and gold, respectively. The need for an event-by-event follow-up (in MC simulations) [52] or an expansion into a few hundred Legendre coefficients with an unreasonably high  $S_n$  quadrature and a few hundred thousand energy groups (in Boltzmann-Fokker-Planck solvers) [53] implies that transport modeling in this sense is unfeasible with current workstation capacities in terms of floating-point operations per second and instructions per second.

Even with advanced MC condensed-history algorithms [24] or Fokker-Planck's operators [54,55] in Boltzmann solvers, albeit to varying degrees, the problem remains time-consuming for clinical deployment. This is true for the uncorrelated Class-I (e.g., MCNP-5 [56] and ITS [57]) and correlated Class-II algorithms (e.g., GEANT-4 [58], Penelope [59], PHITS [60], FLUKA [61], MARS [62], and EGSnrc [63]). Reactor physics models for secondary photons (RPSPs) try to rule out any electronic transport, opting for a partially coupled scheme, which avoids formal charged particle transport while considering their long-range effects. Two motivations seem to be at the origin of their development: (1) even if the energy deposition of charged particles is assumed to be local in some domains, that of bremsstrahlung, annihilation, fluorescence, or relaxation cascades is certainly not, and (2) an RPSP-based scheme should be more realistic than an uncoupled one. A swathe of these methods was introduced in the Los Alamos

MCNP-5 code of 2003, with a thick-target-bremsstrahlung (TTB) model as a default model in photon-mode problems (Mode P) [56]. It was followed by an extension in the VTT (Technical Research Centre of Finland Ltd) SERPENT-2 code in 2016 with annihilation, atomic relaxation, and simplified TTB models [64]. An identical implementation was performed in the MIT OpenMC code in 2018 [65]. First, the potential, the impact, and the limits of such models have never been the subject of investigations. Second, the wider scientific community, alerted to the need for coupled schemes, does not seem aware of the existence of such models. This paper targets (1) the introduction of state-of-the-art RPSPs to the wider scientific community, (2) quantification of their contributions in radiation oncology, in reactor physics, and in a multidisciplinary context, and (3) quantification of their accuracy and CPU time compared with a fully coupled scheme.

## II. MATERIALS AND METHODS

Here, SERPENT-2 (V-2.1.32) [66] is the MC code used for the partially coupled three-dimensional (3D) transport model (the RPSP), while GEANT-4 (V-4.10.07.p01) [58] is the reference MC code used for the fully coupled 3D model. SERPENT-2 is a versatile reactor-physics code, best described as a continuous-energy MC reactor-physics burnup calculation code. The development of SERPENT started in 2004 under the working title of VTT's Probabilistic Scattering Game with the Woodcock neutron delta-tracking algorithm [67]. SERPENT was first publicly presented in 2005 [68], and then revised, summarized, and structured with the publication of Leppänen's thesis [69]. It was developed with two goals in mind: (1) unlike general-purpose MC codes, it was particularly refined for nuclear-reactor lattice calculations, and (2) it was particularly designed to be *as user-friendly as possible*. These two aspects are at the origin of its active growing nuclear user community, distributed across more than 100 organizations and research laboratories in 28 different countries. SERPENT-2 is known for  $k_{\text{eff}}$ -eigenvalue criticality calculations, group constants, generation of scattering matrices and diffusion coefficients [70], spatial homogenization [71], fuel-cycle calculations [72], point-kinetics studies [66], dynamic transient simulations [70], and multiphysics coupling [73–75]. A RPSP-based photon-transport capability was added in 2015 (V-2.1.24), targeting problems related to nuclear-reactor shielding and gamma heating. In the following year, a radioactive source was added to its source bank [76]. Neutron-photon coupling was achieved in 2017 [77], an extension of the TTB model was proposed for  $\beta^\mp$  particles in 2018 [78], and an advanced treatment of energy deposition for RPSP-based transport was proposed in 2019 [79]. One should mention that the user-friendliness offered by the FLUKA graphical user interface (FLAIR) [80]

remains superior to the current user-friendliness level of SERPENT-2.

GEANT-4 is an object-oriented hadronic, electromagnetic, and optical Monte Carlo transport toolkit, which was developed by the worldwide RD44 collaboration before its first public production in 1998 [81] after receiving approval from the CERN Development Committee. Class encapsulation and polymorphism have allowed GEANT-4 to be operational to its full extent and to be continuously refined depending on the needs of the growing communities that have been created around it [82], particularly in the fields of high-energy physics (LHC [83]), space research (ESA [84] and NASA [85]), radiotherapy [86,87], microdosimetry [88–90], radiation protection [91], and more recently biochemistry, materials science [92], and nondestructive testing [93].

A certain similarity between SERPENT-2's photonic models [94] and Salvat's implementation in Penelope [59] can be noticed. Such a similarity is valuable, given that the state-of-the-art nuclear and atomic data (EPICS-2017) have emerged from a compliance operation between EPICS-2014 and Penelope models [95–97]. Therefore, we opt for the G4EmPenelope Physics List [98] in GEANT-4 application development for photon, electron, and positron interactions. The photonic processes considered are photoelectric (G4PenelopePhotoElectricModel), Rayleigh (G4PenelopeRayleighModel), Compton (G4PenelopeComptonModel), and pair and triplet production effects (G4PenelopeGammaConversion). The electronic processes considered are ionization (G4PenelopeIonization), bremsstrahlung (G4PenelopeBremsstrahlung), Urban multiple-scattering (G4UrbanMscModel), and in-flight-positron-annihilation effects (G4PenelopeAnnihilation).

### A. Nuclear-reactor-physics models for secondary photons

Here, we call a transport scheme in which no charged particles are transported, while secondary photons from bremsstrahlung, annihilation, and relaxation cascades are recovered and added to the transport tail, an RPSP-based scheme. In what follows, the state of the art of the most complete implementation of these models is discussed.

#### 1. Thick-target bremsstrahlung

The TTB approximation is introduced to recover positronic and electronic bremsstrahlung radiation. The TTB model, as implemented in MCNP-5, MCNP-6, SERPENT-2, and OpenMC, is based on three assumptions:

- A1.  $\hat{\Omega}_\gamma = \hat{\Omega}'_{e^\mp}$ , i.e., the bremsstrahlung photon inherits the charged particle's incidence direction.
- A2.  $\vec{r}_\gamma = \vec{r}'_{e^\mp}$ , i.e., the bremsstrahlung photon originates at the charged particle's point of birth.

A3. The continuous-slowing-down approximation (CSDA) can be used to assess the yield and energy distribution of the photons.

The assumptions A1–A3 are a legacy of the undocumented implementation of TTB in MCNP-5 and MCNP-6. Although A2 can be legitimate because the goal is to prohibit any transport of charged particles, A1 could have been improved with an angular differential scattering cross section (DSC) similar to the partial-wave shape distribution in G4PenelopeBremsstrahlung. A1 restricts the application of TTB to systems in which electron emission is isotropic, while A2 requires that electrons lose their energy essentially within the material in which they are born. A3 is likely to exclude the application of TTB to catastrophic environments in which the CSDA no longer applies. A3 also implies that the inferred quantities are averages, and thus fluctuations are ignored. Unlike MCNP-5 and MCNP-6, SERPENT-2's TTB model does not confuse positronic and electronic bremsstrahlung. To expand A3, SERPENT-2 uses the CSDA range ( $R_{e^\mp}$ ) as the basis of the TTB model:

$$\begin{aligned} R_{e^\mp} &= \int_0^{E_{e^\mp}} dE'_{e^\mp} \left( \frac{dE'_{e^\mp}}{ds_{e^\mp}} \right)^{-1}, \\ R_{e^\mp} &= \int_0^{E_{e^\mp}} \frac{dE'_{e^\mp}}{S_{\text{rad}}(E'_{e^\mp}) + S_{\text{col}}(E'_{e^\mp})}. \end{aligned} \quad (1)$$

Here,  $E'_{e^\mp}$  and  $E_{e^\mp}$  refer to the initial and final energies, respectively, of the incident charged particle,  $ds_{e^\mp}$  is its travel distance, and  $S_{\text{rad}}$ ,  $S_{\text{col}}$ , and  $S_{\text{tot}}$  denote the radiative, collisional, and total stopping powers, respectively. Equation (1) is used to deduce the bremsstrahlung photon energy:

$$\begin{aligned} E_\gamma(E_{e^\mp}) &= \int_0^{R_{e^\mp}} ds_{e^\mp} \left( \frac{dE'_{e^\mp}}{ds_{e^\mp}} \right)_{\text{rad}}, \\ E_\gamma(E_{e^\mp}) &= \int_0^{E_{e^\mp}} dE'_{e^\mp} \left( \frac{dE'_{e^\mp}}{ds_{e^\mp}} \right)_{\text{rad}} \left( \frac{dE'_{e^\mp}}{ds_{e^\mp}} \right)_{\text{tot}}^{-1}, \\ E_\gamma(E_{e^\mp}) &= \int_0^{E'_{e^\mp}} dE'_{e^\mp} \frac{S_{\text{rad}}(E'_{e^\mp})}{S_{\text{tot}}(E'_{e^\mp})}. \end{aligned} \quad (2)$$

From Eq. (2), one can write the radiative yield as  $Y_{\text{rad}} = E_\gamma(E_{e^\mp})/E_{e^\mp}$ . The algorithm is initialized by calculating the energy DSC and the total-stopping-power tables. In SERPENT-2, Berger *et al.*'s data [99] (from the NIST ESTAR database) were used for both collisional and radiative stopping powers. Recently [77,94], positron and electron collisional stopping powers have been assessed separately with the use of the Sternheimer-corrected [100] Bethe collisional stopping power [101]. The latter correction represents density effects. Exactly as is the case with

G4PenelopeBremsstrahlung, SERPENT-2 uses Kim *et al.*'s  $F_p$  ratio [102] to convert electronic radiative stopping powers and DSCs into positronic ones. The energy DSC is written as

$$\frac{d\Sigma_{\text{br}}}{dE_\gamma} = \frac{Z^2}{\beta_{e^\mp}^2} \frac{1}{E_\gamma} \chi(Z, E'_{e^\mp}, E_\gamma). \quad (3)$$

Salvat's dense  $E'_{e^-}$  grid tabulation [59] is used for the scaled bremsstrahlung DSC ( $\chi$ ). SERPENT-2 performs a logarithmic cubic spline interpolation to form a set of 32 values of  $E_\gamma$  for each  $E'_{e^-}$ .  $\beta_{e^-}$  is the velocity of the incident electron in units of the speed of light. The macroscopic bremsstrahlung cross section ( $\Sigma_{\text{br}}$ ) is obtained after integration of Eq. (3). Expensive interpolation of the bremsstrahlung spectrum is avoided at  $E'_{e^\mp}$  using point probabilities. The second step is to sample the number of bremsstrahlung photons emitted during the slowing down of the charged particles. If  $\Xi_n^\gamma$  is the photon-number yield between  $E_{\text{cut}}$  and  $E'_{e^\mp}$ , then

$$\begin{aligned} \Xi_n^\gamma(E'_{e^\mp}, E_{\text{cut}}) &= \int_{R_{e^\mp}(E_{\text{cut}})}^{R(E_{e^\mp})} ds_{e^\mp} \Sigma_{\text{br}}(E''_{e^\mp}, E_{\text{cut}}), \\ \Xi_n^\gamma(E'_{e^\mp}, E_{\text{cut}}) &= \int_{E_{\text{cut}}}^{E'_{e^\mp}} dE''_{e^\mp} \frac{\Sigma_{\text{br}}(E''_{e^\mp}, E_{\text{cut}})}{S_{\text{rad}}(E''_{e^\mp}) + S_{\text{col}}(E''_{e^\mp})}, \end{aligned} \quad (4)$$

where  $E_{\text{cut}}$  is the bremsstrahlung infrared-divergence cut-off. Equation (4) is used to quantify the energy spectrum of the bremsstrahlung photons, e.g., the number of photons emitted in  $[E_\gamma^1, E_\gamma^2]$  is  $\Xi_n^\gamma(E'_{e^\mp}, E_\gamma^1) - \Xi_n^\gamma(E'_{e^\mp}, E_\gamma^2)$ . The number of bremsstrahlung photons is given by the floor function:

$$N_\gamma = \lfloor \Xi_n^\gamma(E'_{e^\mp}, E_{\text{cut}}) + \xi \rfloor, \forall \xi \in \text{unif}(0, 1). \quad (5)$$

The locally deposited energy during a TTB event is

$$E_{\text{dep}}^{\text{TTB}} = E'_{e^\mp} - \sum_{k=1}^{N_\gamma} E_{\gamma,k}. \quad (6)$$

Equation (6) recalls what was announced at the beginning of this section, that the state-of-the-art TTB approximation requires that the charged particle's range should be lower than the thickness of the material being traversed. This can be problematic in the vicinity of an interface and for thin low- $Z$  materials. For both compounds and mixtures, Bragg's additivity rule is used for both the DSC and the stopping powers [64].

## 2. Annihilation

The model considers only the dominant two-photon electron-positron annihilation mechanism at rest. Three

assumptions are made: (1) both nuclear-recoil and electron-binding effects are ignored, (2) photons are emitted isotropically in opposite directions, and (3) positrons are not transported up to the site of complete thermalization. The first assumption results in the assumption of two 511-keV photons. Ignoring in-flight  $2\gamma$  annihilation is in agreement with the behavior of Heitler's cross section [103]. The third assumption implies that the photons are emitted exactly at the birth site of the pair. Also, remaining vacancies are ignored in this case, since only outer-shell electrons are generally involved in the annihilation process.

### 3. Atomic relaxation cascade

In this study, an atom is left in an excited state (i.e., with a vacancy) after ionization (for electron transport), photoelectric, and Compton effects (for photon transport). Therefore, an outer electron drops, down filling the vacancy, leading to a shower of fluorescence, Auger, Coster-Kronig, and super-Coster-Kronig effects. Both SERPENT-2 and GEANT-4 use [94,104–107] the Evaluated Atomic Data Library-91 (EADL-91) [108]. The latter is limited to elemental, cold, neutral, and isolated atoms. Initially excited or ionized atoms are thus excluded. It is also assumed that the binding energies of all subshells of an ionized atom are identical to those of the neutral ground-state atom. Conjointly, for outer subshells and for all atoms from  $Z = 1$  to  $Z = 5$ , EADL-91 requires local binding-energy deposition for nonradiative transitions. This means that nonradiative transition probabilities are explicit only for  $Z = 6$  to 100 for the  $K$ ,  $L$ ,  $M$ , and  $N$  shells and some  $O$  subshells. The  $O$ ,  $P$ , and  $Q$  radiative transition probabilities are of the order of approximately 0.1%, i.e., smaller than their known accuracy. For both SERPENT-2 and GEANT-4, the relaxation cascade begins with a check of whether the vacancy is provided in the EADL libraries. In this case, an outer subshell is randomly selected based on the transition probabilities. Otherwise, the binding energy of the ionized shell is deposited locally. In SERPENT-2, Walker's sampling technique, which is particularly suited to discrete distributions, is used for this sampling. For nonradiative transitions, two random selections are made, one for the transition electron to the original vacancy and the other for the shell generating the Auger electron. If the energy of the selected transition is greater than the cutoff energy (in SERPENT-2) or that for production of secondaries (in GEANT-4), a photon (or an electron) is emitted isotropically. The procedure is restarted from the beginning for the new vacancy (in the radiative case) and the two new vacancies (in the nonradiative case). Figure 1 shows a simplified flowchart of the RPSP-based scheme.

#### B. Thresholds

For SERPENT-2, there is one cutoff ( $E_{\text{cut}}$ ), that for transport (set `ecut`), which is also used as a

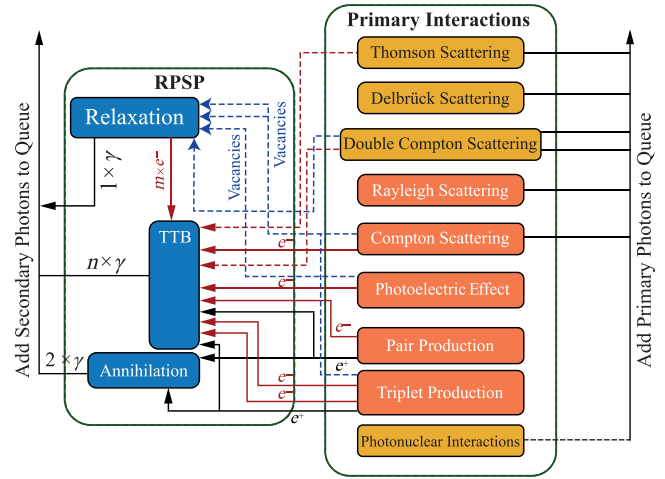


FIG. 1. Simplified flowchart of the RPSP-based scheme. Thomson, Delbrück, and double Compton scattering and photonuclear interactions are neglected. RPSPs are triggered just after the primary-photon interactions. Cascades are triggered by Compton scattering, the photoelectric effect, and triplet production.  $m$  and  $l$  refer to the numbers of Auger electrons and fluorescence photons, respectively.  $n$  is the number of bremsstrahlung photons. Triplet production, neglected in SERPENT-2, is taken into account in the reference GEANT-4 scheme.

secondary production threshold. We use the lowest possible value, the default 1-keV cutoff, adhering to Cullen's recommendations for the EPCIS-1991, 1997, 2014, and 2017 data [109]. For GEANT-4, there are at least three cutoffs that can be specified. First, there is a transport cutoff, fixed in this study at 1 keV for photons, electrons, and positrons. Second, the Class-II CH algorithm (`G4UrbanMscModel`) requires a secondary production threshold ( $E_s$ ) in terms of particle range. The latter is internally converted to energy for each material type. Here, unlike in the classic approach, these thresholds are specified in energy units, i.e., a 1-keV threshold for all materials. This ensures total compliance with SERPENT-2's scheme. Third, there is a final Boolean-type threshold ( $E_{\text{cut}}^{\text{cas}}$ ), `SetDeexcitationIgnoreCut`, which, when activated, generates all possible relaxations and transports all the particles emitted even if their energies are well below the production threshold and the transport cutoff. The last two thresholds imply that  $\delta$  rays, bremsstrahlung photons, fluorescence photons, and Auger electrons (below 1 keV) are not emitted. Consequently, the process is treated with the CSDA (for ionization and bremsstrahlung) or with local energy deposition (for relaxation).

## III. RESULTS AND DISCUSSION

### A. Impact of RPSPs in a medical-physics context

Here, the Rogers and Mohan (RM) multislab benchmark [110], known for patient treatment planning for radiotherapy, is used for the medical study. A unidirectional (or

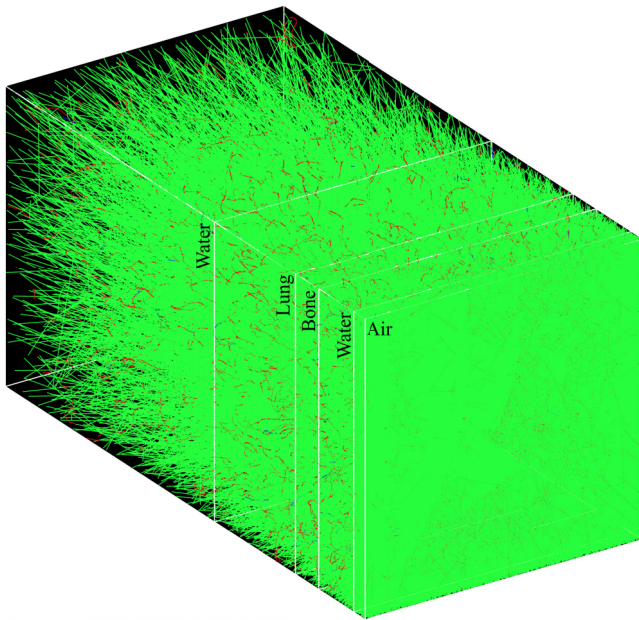


FIG. 2. Rogers and Mohan geometry. From right to left, the materials are air (1 cm), water (3 cm), compact bone (2 cm), lung (7 cm), and water (18 cm). The material compositions are those assumed by NIST. All slabs have equal heights and widths of 16 cm. The source is volumetric  $[(0.5 \times 16 \times 16) \text{ cm}^3]$  and unidirectional (or isotropic), sampled in air, starting at the origin of the axes. Photon, electron, and positron tracks are shown in green, red, and blue, respectively. Only 30 000 events are shown. For a unidirectional (isotropic) source,  $70 \times 10^6$  ( $300 \times 10^6$ ) events are considered for a 0.1% standard deviation. No quantitative information is to be inferred from this figure.

isotropic) source irradiates a slab of water, followed by bone and lung tissues, and a final water slab (Fig. 2). A wide range of energies (low, medium, and relatively high) is considered for three reasons: (1) to cover typical sources used in brachytherapy, (2) to span the spectrum of typical megavoltage clinical beams used in external radiotherapy, and (3) to detect the typical threshold for which an uncoupled or partially coupled transport scheme is no longer sufficient. For any material and any beam studied, the standard deviation required for statistical convergence is fixed at 0.1% everywhere. From Sec. II A, we recall that TTB is not applicable to the RM benchmark for unidirectional beams. The source anisotropy and the high heterogeneity of the benchmark, combined with the reduced slab thicknesses and the low-density and low- $Z$  materials, interfere with both approximations A1 and A2, thus implying this exclusion. Otherwise, for all other benchmarks, TTB is activated.

### 1. Monoenergetic photon beams incident on Rogers and Mohan benchmark

Figures 3(a) and 3(b) show, for unidirectional beams, the depth-dose curves and SERPENT-2 percentage errors for

the two models with respect to the fully coupled GEANT-4 scheme ( $G4-[\gamma, e^-, e^+]$ ). The latter, which is qualified to less than 0.1% deviation from experimental data, is referred to here as the reference scheme. Three observations can be made.

(a) *First, the time-consuming fully coupled scheme is not required everywhere for any energy, except for buildup and interfaces.* The current focus in clinical routine is on the within-tissue dose accuracy. For brachytherapy, the within-tissue RPSP mean errors are 0.30, 0.42, 0.027, 0.14, 0.0088, and 0.0074% for palladium-103, iodine-125, iridium-192, cesium-137, 1-MeV, and cobalt-60 sources, respectively. With increasing energy, the corresponding error does not exceed 0.2, 0.5, 0.6, 0.7, and 0.8% for energies of 2, 3, 4, 5, and 6 MeV, respectively [Fig. 3(b)]. The penalties are located in the buildup region and the bone interfaces. Modeling the buildup requires complete modeling of electronic disequilibrium. The lack of stopping powers and electron-backscattering models leads to the expected inability of SERPENT-2 to handle the dose discontinuity at the bone interface. Conversely, only electron transport can physically correct these two aspects. The buildup and interface penalties are emphasized with increasing energy, since the range of charged particles is accordingly increased. The buildup failure spans 0.75, 1.25, 1.85, 2.15, and 3.15 cm for energies of 2, 3, 4, 5, and 6 MeV [Fig. 3(a)]. In turn, one can see that, in the event of buildup and interface disparities, the latter shapes are clearly systematic and can be manipulated by a correction function [Fig. 3(a)]. The extent of the latter observation within a patient's anatomy requires further investigation. Backscattering effects are difficult to distinguish at the lung-water interface due to the density equivalence ( $1.05$  vs  $1.00 \text{ g/cm}^3$ ) of these two materials.

(b) *Second, defining a beam energy threshold for a fully coupled scheme, where needed, is possible.* In clinical routine, electronic equilibrium is assumed everywhere. This means that buildup and interface effects are not of current interest. For all energies studied, the within-tissue deviation of the RPSP predictions from GEANT-4 remains below 1.3% [Fig. 3(b)]. It is shown in Sec. III A 2 that this result cannot be achieved without RPSPs. Accordingly, in complete compliance with both the AAPM's 2% criterion and current clinical-practice guidelines, we conclude that RPSPs are qualified for treatment planning for brachytherapy and, potentially, external radiotherapy.

(c) *Third, the RPSP-based scheme results in a substantial gain in terms of CPU-time usage.* Table I lists, for a statistical uncertainty of 0.1%, the CPU times for GEANT-4 and SERPENT-2 on a 3.8-GHz Intel Core i7 processor. Even with the default (unrefined) CH algorithm, electron transport entails that (1) the GEANT-4 CPU time is measured in several days (versus approximately 3 h for SERPENT-2), and (2) the GEANT-4 computational scheme becomes even more

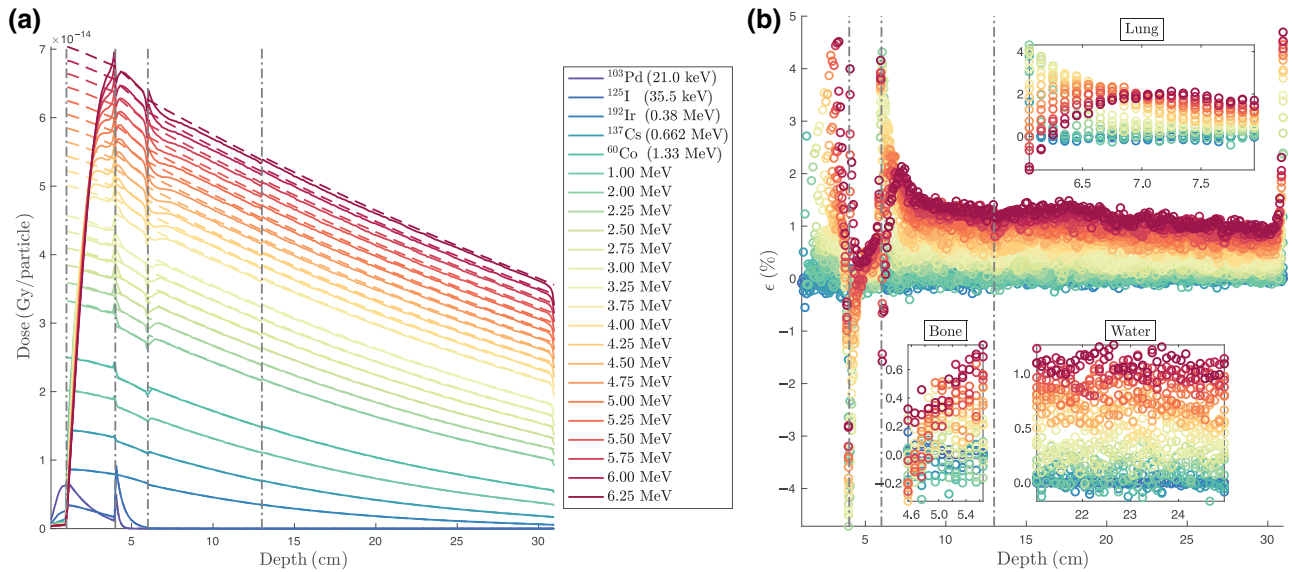


FIG. 3. Incident unidirectional and monoenergetic photon beams on Rogers and Mohan benchmark: (a) depth-dose distributions (dashed lines, S2-[RPSP]; solid lines, G4-[ $\gamma, e^-, e^+$ ]); (b) relative error of the S2-[RPSP] scheme with respect to the reference G4-[ $\gamma, e^-, e^+$ ] scheme. On the right, we focus on the error inside the materials, i.e., excluding the buildup region.

time-consuming with increasing energy (versus strong stability for SERPENT-2). The RPSP scheme results in savings of 58 to 78 in CPU-time magnitude at 3 and 6 MeV, respectively. The increase in CPU time between 1.33 and 6 MeV is 8 days for GEANT-4 versus only 18 min for SERPENT-2. With multithreading, convergence acceleration techniques, and a lower uncertainty criterion, there is a good chance for an additional optimization effort to achieve a CPU time of clinical interest for the RPSP-based scheme, as is the case with MC variance reduction techniques [111,112].

Figure 4 shows the corresponding profiles for an isotropic source. The latter allows the activation of TTB. Massive tests show that TTB is mandatory; otherwise, the errors are 1% higher above 3 MeV. Interest in this source is limited to brachytherapy. Figure 4(a) shows that the buildup failure remains present. However, the interface backscattering errors are on the decline. The correspondence with respect to the reference scheme is consequently further improved within tissues [Fig. 4(b)]; systematic reductions of a 0.25% difference from Fig. 3 are observed in the bone, lung, and second water layerings.

TABLE I. CPU times for the fully coupled scheme (GEANT-4) versus the RPSP-based scheme (SERPENT-2) on a 3.8-GHz Intel<sup>®</sup> Core<sup>™</sup>-i7 processor for six representative energies. The standard statistical deviation is below 0.1%.

	$^{60}\text{Co}$	2 MeV	3 MeV	4 MeV	5 MeV	6 MeV
S2-[RPSP]	3.1 h	3.1 h	3.1 h	3.2 h	3.3 h	3.4 h
G4-[ $\gamma, e^-, e^+$ ]	72 h	120 h	180 h	216 h	244 h	264 h

A compensation effect is probably at the origin of this observation. Source isotropy implies  $\hat{\Omega}'$ , random sampling in  $[0, 4\pi]$ . Thus, failure in the dose deposition due to a given backscattering event of a particular incidence angle is immediately cushioned by subsequent deposition with a different anisotropy. The previous conclusions for a unidirectional source are retained, with a possible 5-MeV threshold increase for the coupled scheme.

A step refinement of the condensed-history algorithm was done following the recommendations of Archambault and Mainegra-Hing [113] and Poon and Verhaegen [87]. The CPU time becomes extremely excessive; e.g., for a 3-MeV beam, 2 months are needed versus 180 h for the default G4UrbanMscModel (see Table I). For all tissues, buildup and interface regions included, the discrepancies are less than the accuracy of the cross sections. A 0.2% average deviation is observed. The air slab is the only exception, where we report significant differences of up to 10%. These differences are consistent with the observations of Vilches *et al.* [114], Poon *et al.* [115], and Archambault and Mainegra-Hing [113]. In this study, the air slab has no impact on the dose distribution. We therefore retain the reference unrefined scheme.

## 2. Identification of the impact of RPSPs

To answer the question of whether or not the observed performance is due to the RPSP contribution, we propose, at this level, two other computational schemes: (1) an uncoupled GEANT-4 computational scheme (G4-[ $\gamma$ ]), i.e., only primary photons are transported, while charged particles are eliminated at the moment of birth, and (2)

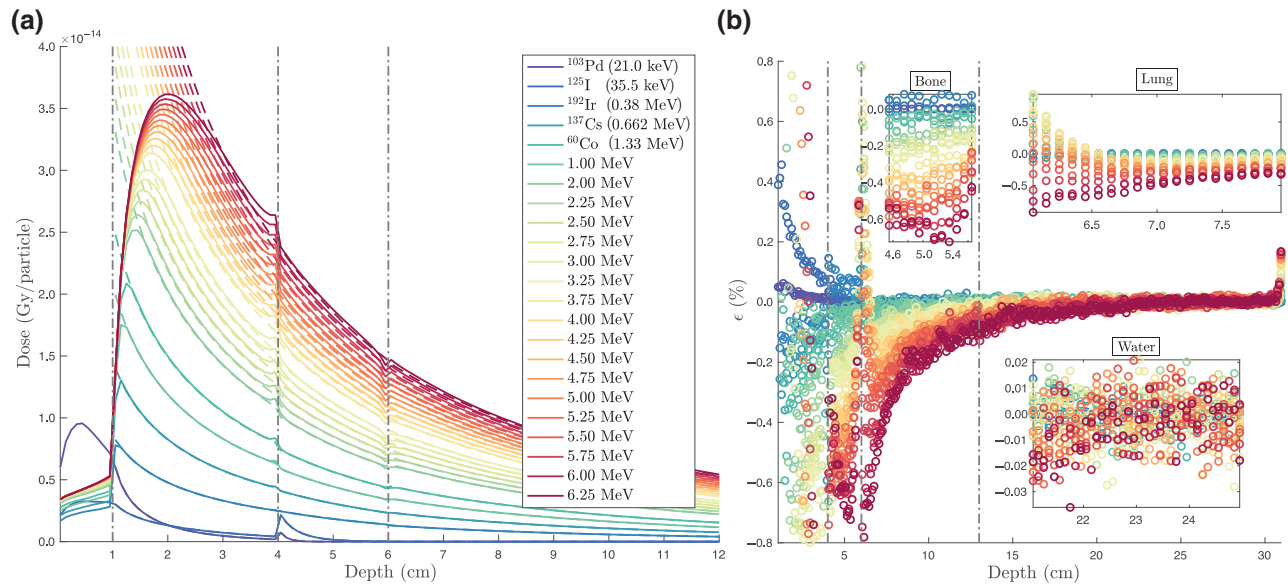


FIG. 4. Isotropic and monoenergetic photonic source irradiating the Rogers and Mohan benchmark: (a) depth-dose distributions (dashed lines, S2-[RPSP]; solid lines, G4- $[\gamma, e^-, e^+]$ ); (b) relative error of the S2-[RPSP] scheme with respect to the reference G4- $[\gamma, e^-, e^+]$  scheme. On the right, we focus on the error inside the materials, i.e., excluding the buildup region.

a special GEANT-4 computational scheme (G4- $[\gamma + \text{ann.}]$ ) similar to the previous scheme, except that the positron is transported, thermalized, and annihilated. Annihilation photons are then recovered and transported. Obviously, as was the case with Liegeard *et al.*'s model [26], relaxation cascades are here assumed one of the three RPSP and will not be activated in the last two cases.

Figures 5(a)–5(d) show the behavior of the relative errors as a function of energy at specific depths in the water layers and in the bone and lung tissues. The spatial behaviors of the same errors are depicted in Figs. 5(e) and 5(f) for 3- and 6-MeV unidirectional beams, respectively. All errors are with respect to the reference G4- $[\gamma, e^-, e^+]$  scheme for the same energy and at the same depth. From Figs. 5(a)–5(d), first, one can see that the RPSPs are the only components responsible for the high correspondence between SERPENT-2 and GEANT-4. If these models are omitted, the G4- $[\gamma]$  scheme shows 2, 12, 6, and 19 times the RPSP error in the water, bone, and lung and the last water slab, respectively, at 3 MeV. These errors rise to 10, 17, 5, and 6 times at 6 MeV. Partial inclusion of one of the RPSPs (with the G4- $[\gamma + \text{ann.}]$  scheme) shows an immediate gain in accuracy, and this is true at any point in space and for any energy.

Secondly, only the RPSP-based scheme guarantees an error below 1.3% within tissues. Otherwise, the errors are higher than the AAPM criterion. Thirdly, the impact of RPSPs is demarcated within the bone tissue. Indeed, Fig. 5(b) highlights a distinct decrease in the deviation of the RPSP scheme from the reference scheme in the bone tissue, although it does not exceed 0.42% at high energies, against an increasing trend in the errors of the uncoupled

scheme. Compared with other materials, there is a similar gain in accuracy in bone with the inclusion of one of the RPSPs (G4- $[\gamma + \text{ann.}]$ ). Bone has higher density than water and lung and contains substantial amounts of  $^{20}\text{Ca}$  (20.993%) and  $^{15}\text{P}$  (10.497%), which confer a higher effective  $Z$ . However, when the latter increases, pair (and triplet) production becomes more probable. The same is true for atomic relaxation and bremsstrahlung. This behavior points to the idea that the impact of RPSPs should be greater for denser and higher- $Z$  materials, such as prostheses. Fourthly, from Figs. 5(e) and 5(f), it appears that the impact of RPSPs is systematic, observed at all depths, and can be verified at any point in space. In summary, at 6 MeV, the error of the uncoupled scheme is found to be 4.5 times that of the RPSP scheme in water and lung, and 11 times that of the RPSP scheme in bone. The impact of RPSPs stands just above the annihilation threshold, and increases quickly with both energy and  $Z$ . Finally, an improved accuracy gain is possible with revisiting of the TTB model for unidirectional beams.

### 3. Effects of cutoffs on quantification of the impact of RPSPs

Here, we are interested in evaluating whether or not the transport cutoff and the secondary-production and relaxation thresholds imposed on the reference G4- $[\gamma, e^-, e^+]$  scheme (Sec. II B) could have influenced the previous study. More complete GEANT-4 schemes are then introduced to test this hypothesis. Five computational schemes, examining different combinations of cutoff energies and production thresholds, are summarized in Table II. The  $G_0$



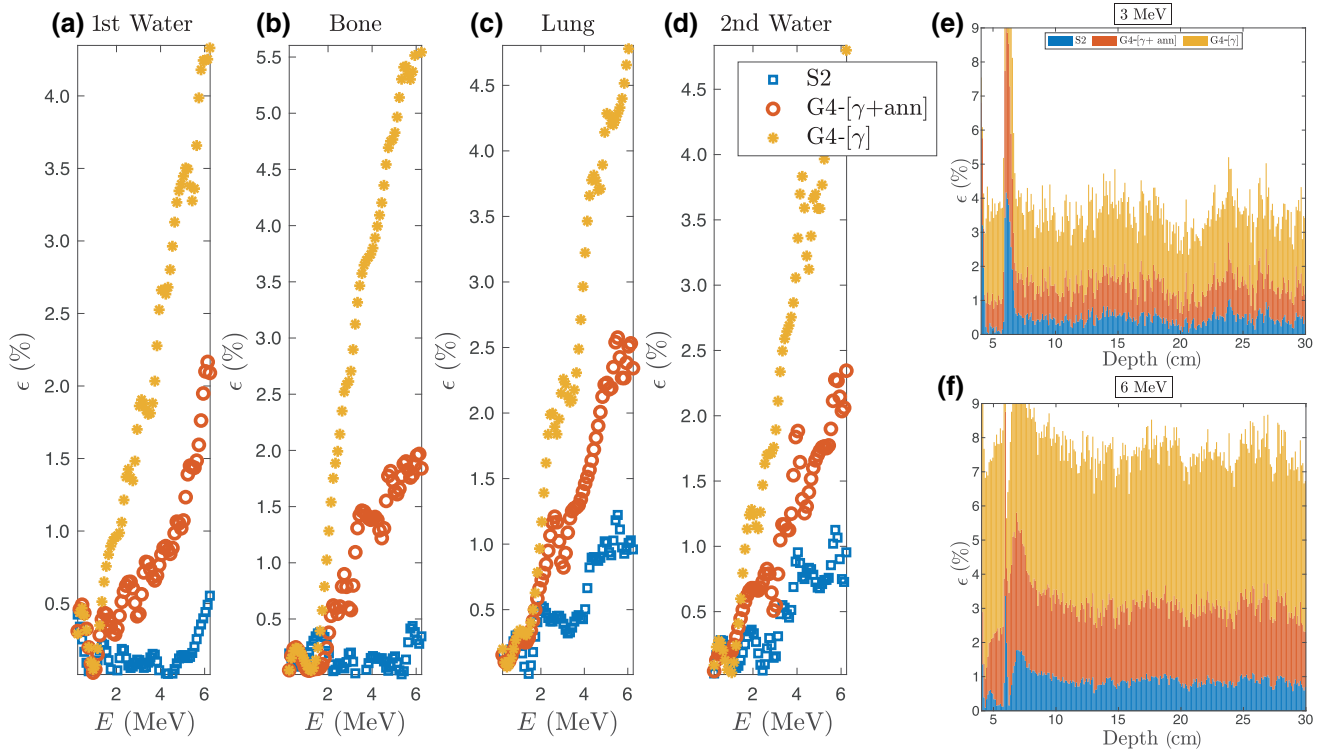


FIG. 5. Incident unidirectional and monoenergetic photon beams on Rogers and Mohan benchmark: (a)–(d) Percentage errors of S2-[RPSP], G4-[ $\gamma$  + ann.], and G4-[ $\gamma$ ] schemes versus energy at 3.0 cm (water), 5.2 cm (bone), 9.0 cm (lung), and 20.0 cm (water); (e) percentage errors of spatial behavior of S2-[RPSP], G4-[ $\gamma$  + ann.], and G4-[ $\gamma$ ] schemes. All errors are evaluated with respect to the reference G4-[ $\gamma$ ,  $e^-$ ,  $e^+$ ] scheme.

scheme corresponds to the starting reference scheme. The thresholds labeled “GEANT-4” in Table II refer to GEANT-4’s default values. These are therefore range-production thresholds and range cutoffs, resulting in 990-eV limits for all materials here. The 100-eV cutoff is Cullen’s accuracy limit on the Evaluated Nuclear Data Files (ENDF) cross sections. In the case of unlimited cascades, all fluorescence photons and Auger electrons, subject to an emission probability, are emitted and transported, even if the binding energy is below the threshold of 1 keV, 990 eV, or 100 eV.

TABLE II. Summary of optimized GEANT-4 studies with different state-of-the-art transport cutoffs ( $E_{\text{cut}}$ ) and secondary-production ( $E_s$ ) and relaxation ( $E_{\text{cut}}^{\text{cas}}$ ) thresholds. For all of the studies  $G_0$ – $G_5$ , the upper limit of the standard deviation is limited to 0.1%. Brem., bremsstrahlung; PIXE, charged-particle-induced x-ray emission.

Scheme	$E_{\text{cut}}$	$E_s$	Brem.	PIXE	Cascades	$E_{\text{cut}}^{\text{cas}}$
$G_0$	1 keV	1 keV	Yes	No	Yes	1 keV
$G_1$	1 keV	GEANT-4	Yes	No	Yes	Unlimited
$G_2$	1 keV	GEANT-4	Yes	No	Yes	GEANT-4
$G_3$	1 keV	1 keV	Yes	Yes	Yes	Unlimited
$G_4$	1 keV	1 keV	No	No	No	
$G_5$	100 eV	100 eV	Yes	No	Yes	Unlimited

“PIXE” refers to the recent models in GEANT-4 for charged-particle-induced x-ray emission [116]. Figure 6 shows the relative error of the RPSP-based scheme with respect to

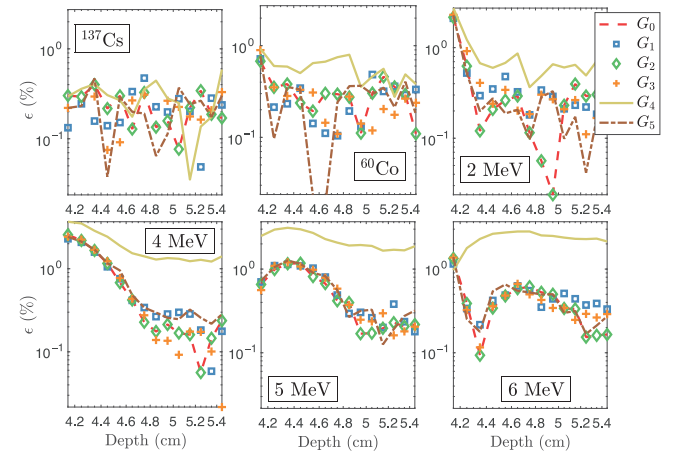


FIG. 6. Effect of transport cutoff and secondary production and relaxation thresholds on quantification of the impact of RPSPs. The plots show the percentage dose error of SERPENT-2 with respect to the optimized schemes  $G_0$ – $G_5$ .  $G_0$  is the reference G4-[ $\gamma$ ,  $e^-$ ,  $e^+$ ] scheme. The schemes  $G_1$ – $G_5$  are summarized in Table II.

the schemes  $G_0$ – $G_5$ . For all the energies studied, regardless of depth, refinement of the cutoffs and thresholds has no significant effect on the reference dose. The deviations are within the range of statistical fluctuations. Only the complete exclusion of an elementary phenomenon, such as relaxation or bremsstrahlung, could impact the result (see the  $G_4$  case).

### B. Multidisciplinary impact of RPSPs

The dimensions of the 3D RM benchmark are kept, while unidirectional photon beams now irradiate homogeneous slabs. The irradiated materials include  ${}^4\text{Be}$ ,  ${}^6\text{C}$ ,  ${}^{13}\text{Al}$ ,  ${}^{26}\text{Fe}$ ,  ${}^{29}\text{Cu}$ ,  ${}^{32}\text{Ge}$ ,  ${}^{47}\text{Ag}$ ,  ${}^{79}\text{Au}$ ,  ${}^{82}\text{Pb}$ , and  ${}^{92}\text{U}$ . The corresponding NIST densities are used. The choice of these atoms is aimed at covering a wide range of materials of ascending  $Z$  and density. Figure 7 shows a comparison of depth-dose curves at 3 MeV between the RPSP-based scheme and  $G4$ - $[\gamma, e^-, e^+]$ . Except for limited buildup regions, the discrepancies are lower than 0.3% everywhere. Moreover, these discrepancies remain below 1.0% in most cases at 6 MeV. The relative errors of the  $S2$ -[TTB=1],

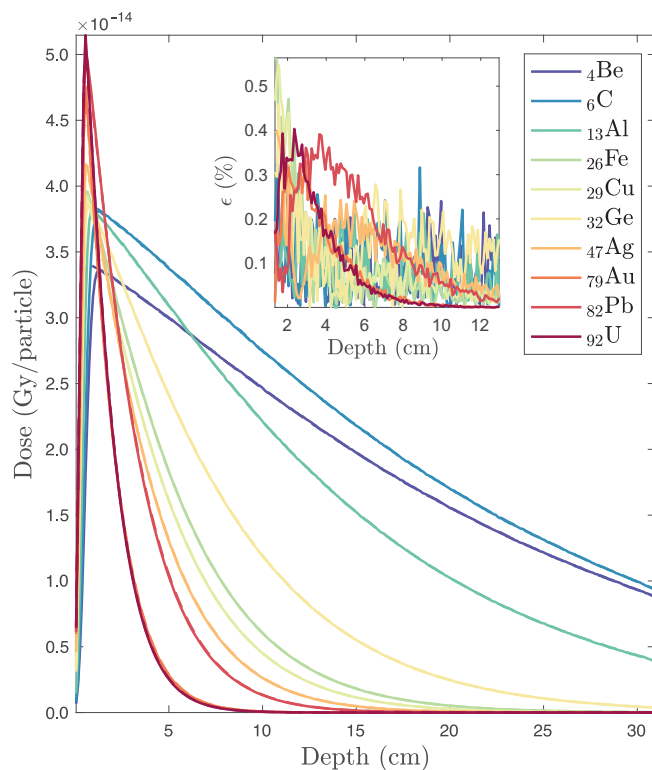


FIG. 7. Depth-dose curves for the RPSP-based scheme (dashed lines) compared with the reference  $G4$ - $[\gamma, e^-, e^+]$  scheme (solid lines) for a 3-MeV unidirectional photon beam incident on homogeneous slabs of  ${}^4\text{Be}$ ,  ${}^6\text{C}$ ,  ${}^{13}\text{Al}$ ,  ${}^{26}\text{Fe}$ ,  ${}^{29}\text{Cu}$ ,  ${}^{32}\text{Ge}$ ,  ${}^{47}\text{Ag}$ ,  ${}^{79}\text{Au}$ ,  ${}^{82}\text{Pb}$ , and  ${}^{92}\text{U}$ . The dimensions of the irradiated slab are  $(30 \times 16 \times 16)$   $\text{cm}^3$ . Convergence is obtained for a 0.1% mean standard deviation. The inset shows the relative error of the RPSP-based scheme with respect to the reference scheme.

TABLE III. Errors at  $d_{\text{max}}$  compared with the reference  $G4$ - $[\gamma, e^-, e^+]$  scheme for a 6-MeV unidirectional beam on homogeneous slabs.

Atoms	S2-[RPSP]	S2-[TTB=0]	G4- $[\gamma + \text{ann.}]$	G4- $[\gamma]$
${}^4\text{Be}$	0.466	1.410	1.276	2.817
${}^6\text{C}$	0.767	2.124	1.757	3.784
${}^{13}\text{Al}$	0.767	2.124	1.757	3.784
${}^{26}\text{Fe}$	0.767	2.124	1.757	3.784
${}^{29}\text{Cu}$	0.944	3.377	2.424	7.332
${}^{32}\text{Ge}$	0.302	5.391	4.047	10.284
${}^{47}\text{Ag}$	0.302	5.391	4.047	10.284
${}^{79}\text{Au}$	0.899	5.653	3.918	8.256
${}^{82}\text{Pb}$	1.667	5.418	3.706	8.257
${}^{92}\text{U}$	0.975	5.763	4.068	7.777

$S2$ -[TTB=0],  $G4$ - $[\gamma]$ , and  $G4$ - $[\gamma + \text{ann.}]$  schemes as a function of energy are depicted in Fig. 8 at  $d_{\text{max}}$  (the depth of maximum dose). The errors are with respect to the reference  $G4$ - $[\gamma, e^-, e^+]$  scheme. First, one can see that only complete inclusion of RPSPs allows an error of the order of 1% or less. Also, one can verify that the inclusion of one of the RPSPs implies a reduction in the systematic error of the current  $G4$ - $[\gamma]$  scheme. At 7 MeV, the  $G4$ - $[\gamma]$  error is 9.6, 10.5, 12.6, and 9.2 times the RPSP error in aluminum, copper, gold, and uranium, respectively. On average, all atoms included, the RPSP error stabilizes at around 0.7% at high energies, in contrast with a behavior of increasing error for all other schemes. For a 6-MeV beam, Table III list the errors of the schemes at depth  $d_{\text{max}}$ . From Table III and Fig. 8, we see that lead shows a jump in the error of the RPSP-based scheme from 0.8% (at 5.75 MeV) to 1.6% (at 6 MeV), which stabilizes around 1.7% (at 7 MeV). This jump is explained by the inability of assumption A3 in the TTB model (Sec. II A) to handle catastrophic collisions in lead. The latter cannot be treated with the CSDA. Kalliaisenaho [94] predicted such a failure of TTB at high  $Z$  above 5 MeV.

Secondly, the hypothesis that the impact of RPSPs is greater as  $Z$  increases holds true overall. There are slight exceptions to this trend. We observe in Fig. 8 that there is a break in the monotonic upward behavior as a function of energy for the  $G4$ - $[\gamma]$  scheme, but also for the  $G4$ - $[\gamma + \text{ann.}]$  and  $S2$ -[TTB=0] schemes. Other than the transport of primary photons, the only common point between these schemes is the absence of a bremsstrahlung model. This break is observed for  ${}^{26}\text{Fe}$  (4.25 MeV),  ${}^{29}\text{Cu}$  (6.25 MeV),  ${}^{32}\text{Ge}$  (7 MeV),  ${}^{47}\text{Ag}$  (3.75 MeV), and  ${}^{82}\text{Pb}$  (6 MeV). This phenomenon cannot therefore be linked to the process of annihilation (see  $G4$ - $[\gamma + \text{ann.}]$  in Fig. 8) nor to that of relaxation (see  $S2$ -[TTB=0] in Fig. 8), which implies by elimination a direct link with the bremsstrahlung process. With increasing energy, the screening effect intensifies. This reduces the rate of radiative collisions and produces a decrease in the deviation

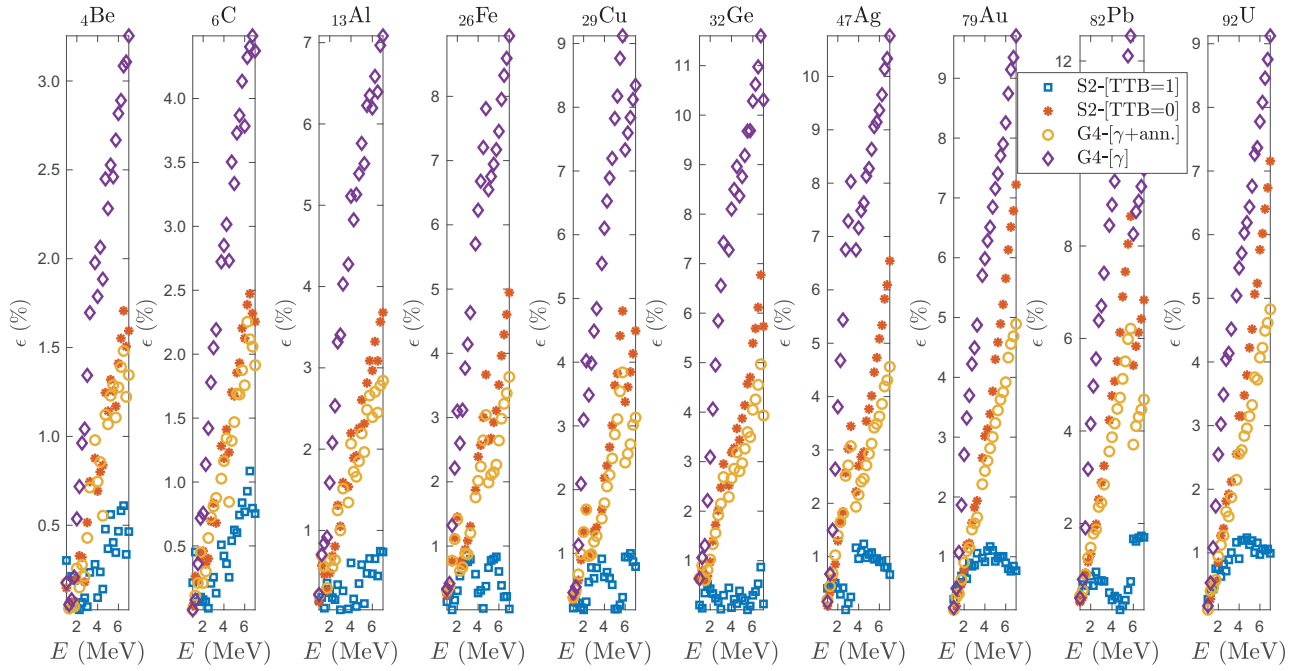


FIG. 8. Energy behavior of S2-[TTB=1] (full RPSP), S2-[TTB=0] (RPSP excluding TTB), G4-[ $\gamma$ ], and G4-[ $\gamma$  + ann.] schemes with respect to the reference G4-[ $\gamma$ ,  $e^-$ ,  $e^+$ ] scheme. All errors are evaluated at the slab's hottest point. Convergence is obtained for a 0.1% mean standard deviation.

from G4-[ $\gamma$ ,  $e^-$ ,  $e^+$ ]. The screening effect is impacted by the structure of the atomic shells.

Figure 9 shows, at 6 MeV for the same models, the depth behavior of the errors from  $d_{\text{max}}$  to  $d_{70}$  (the depth

corresponding to 70% of the maximum dose). All the models end up converging towards the reference G4-[ $\gamma$ ,  $e^-$ ,  $e^+$ ] scheme following complete attenuation in the material. However, one can see that the impact of RPSPs

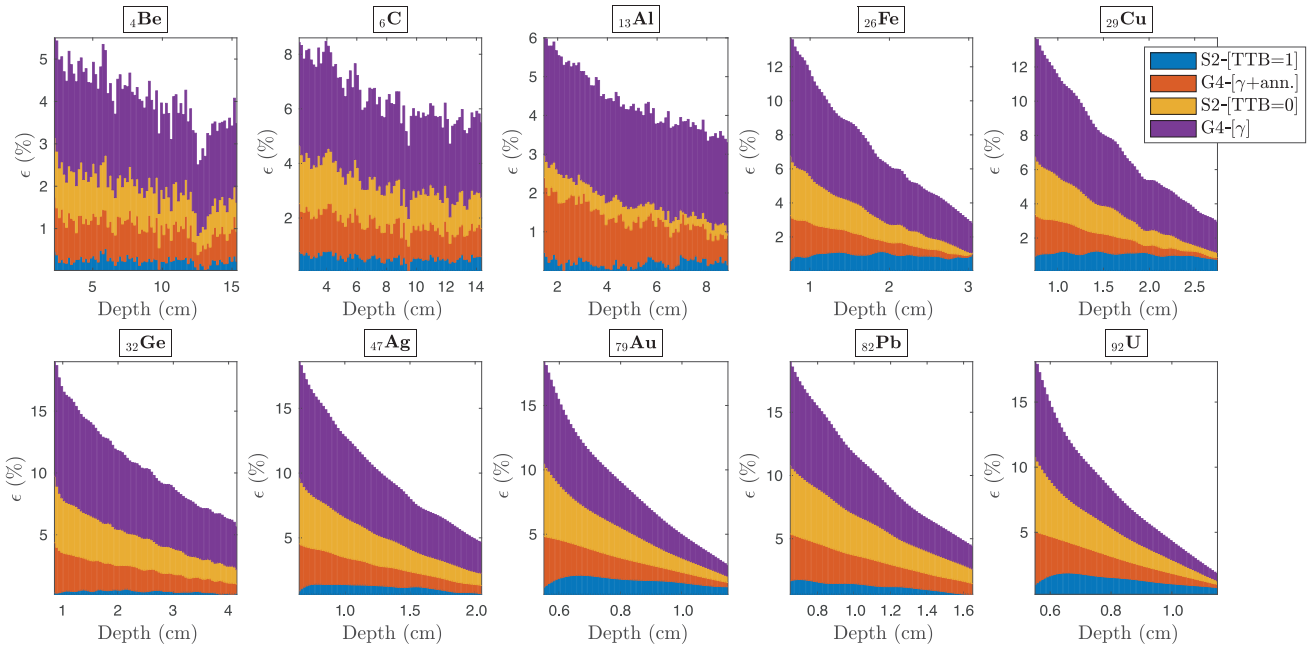


FIG. 9. Spatial behavior of S2-[TTB=1] (full RPSP), S2-[TTB=0] (RPSP excluding TTB), G4-[ $\gamma$ ], and G4-[ $\gamma$  + ann.] schemes with respect to the reference G4-[ $\gamma$ ,  $e^-$ ,  $e^+$ ] scheme at 6 MeV. The domain of the plots is from  $d_{\text{max}}$  (the hottest point) to  $d_{70}$  (the depth corresponding to 70% of the maximum dose). Convergence is obtained for a 0.1% mean standard deviation.

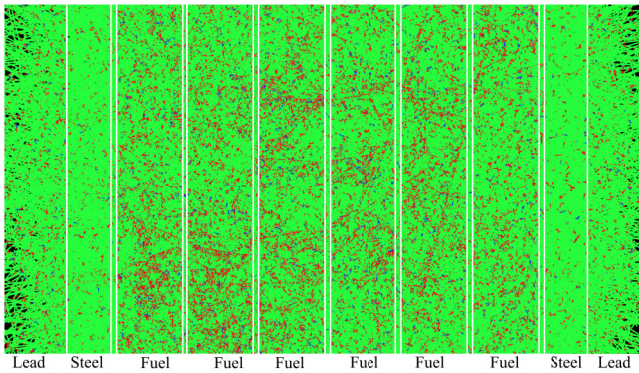


FIG. 10. Simplified multislab reactor benchmark. The compositions of the lead (3 cm), steel (2 cm), fuel (3 cm), and light-water moderator (0.5 cm) slabs are detailed in Table IV. Both UOX and MOX fuels are considered. Since neutrons are not transported, the fission source is assimilated into a 6.6-MeV isotropic volumetric source, uniformly distributed in every fuel region. All slabs have equal heights and widths of 16 cm. Photon, electron, and positron tracks are shown in green, red, and blue, respectively. Only 30 000 events are shown. For all reactor schemes,  $900 \times 10^6$  events are considered for a 0.1% standard deviation.

is demarcated everywhere, and especially at  $d_{\max}$  and its surroundings.

### C. Impact of RPSPs in the reactor-physics context

The last benchmark is a simplified multislab reactor, shown in Fig. 10. The reactor shielding and vessel are represented by lead and steel slabs. Between them, six fuel slabs are separated by light-water moderator slabs. The main role of the latter is to ensure thermalization of the neutrons and removal of fission heat. Typical PWR

TABLE IV. Compositions of materials in multislab reactor benchmark.

Material	Density (g/cm <sup>3</sup> )	Composition (%)
MOX	10.9913	U (83.78), Pu (4.30), Am (0.08), O (11.84)
UOX	10.2841	U (88.15), O (11.85)
Steel	8.060	Fe (64.1922), Cr (18.37), Ni (12.35), Mo (2.386), Mn (1.619), Si (0.5093), Cu (0.1734), W (0.11), Co (0.1052), V (0.0508), C (0.0445), N (0.04), P (0.02), S (0.0175), As (0.01067), Pb (0.001), Bi (0.0004)
Lead	11.35	Pb (100)
Water	1.00	H (88.15), O (11.85)

UOX and MOX fuel slabs are considered here. The composition of these materials is summarized in Table IV. Here, the fission photonic source is assimilated into a 6.6-MeV isotropic volumetric source, uniformly distributed in every fuel region. Liegeard's work was limited to primary photons. Here, we wonder if there is an additional accuracy gain with the inclusion of secondary gammas. This benchmark is therefore a prerequisite for a complete large-scale quantification of the impact on a PWR. Our schemes exclude the neutron component. A complete quantification requires a qualified reactor-physics code (e.g., Dragon-5 [117] or MCNP-6 [118]) with a coupled  $(n, \gamma, e^-, e^+)$  transport capability. Figure 11(a) shows, for the S2-[TTB=1], S2-[TTB=0], G4-[ $\gamma + \text{ann.}$ ], and G4-[ $\gamma$ ] schemes and the reference G4-[ $\gamma, e^-, e^+$ ] scheme, the energy deposition profiles. The percentage errors with respect to the reference scheme are depicted in Fig. 11(b). The isotropy of fission and the density of the fuel mean that the energy

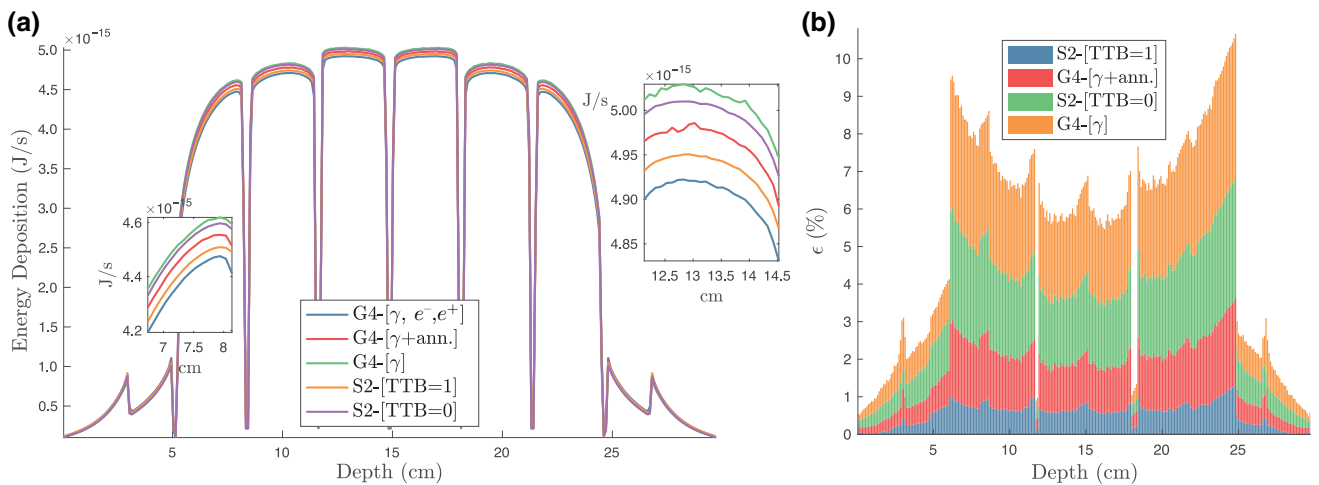


FIG. 11. Simplified multislab reactor benchmark: (a) energy deposition profiles of G4-[ $\gamma, e^-, e^+$ ], G4-[ $\gamma + \text{ann.}$ ], G4-[ $\gamma$ ], S2-[TTB=1], and S2-[TTB=0] schemes; (b) relative errors of G4-[ $\gamma + \text{ann.}$ ], G4-[ $\gamma$ ], S2-[TTB=1], and S2-[TTB=0] with respect to the reference G4-[ $\gamma, e^-, e^+$ ] scheme.

TABLE V. Simplified multislab reactor: average (and maximum) percentage errors with respect to the reference G4- $[\gamma, e^-, e^+]$  scheme. Averages and maxima are taken over the entire volume occupied by the reactor shielding, vessel, and fuel.

	S2-[TTB=1]	S2-[TTB=0]	G4- $[\gamma + \text{ann.}]$	G4- $[\gamma]$
Lead	0.103 (0.407)	0.396 (0.694)	0.289 (0.903)	0.503 (1.543)
Steel	0.428 (1.445)	0.939 (2.008)	0.622 (1.429)	0.856 (1.947)
UOX	0.960 (1.035)	2.519 (3.109)	1.654 (2.130)	2.932 (3.712)
MOX	0.742 (0.815)	2.849 (3.989)	1.972 (2.678)	3.451 (4.853)

deposition is at its maximum in the fuel and is gradually attenuated in the shielding. The energy deposition is minimal, but not zero, in the moderator. This is due, on the one hand, to the volume of the latter, which is very limited with respect to complete photon attenuation, and, on the other hand, to the density of the fuel, which is very high, preventing electron flux escaping (see Fig. 10). Only electrons originating at the periphery of the fuel in the direction of the water slab involve energy deposition in the moderator. Two observations can be made. The first is that the G4- $[\gamma]$  scheme, suggested by Liegeard, implies a systematic overestimation of the PPF, and also of the energy deposition in the fuel, vessel, and shielding. The second is that the inclusion of one of the RPSPs allows convergence towards a more realistic energy deposition profile (shown for G4- $[\gamma, e^-, e^+]$ ). Figure 11(b) shows that the RPSP-based scheme is the only scheme that ensures an error below 1.04% everywhere, inside the core, vessel, and shielding of the reactor. The PPF overestimation of the uncoupled G4- $[\gamma]$  scheme is 2.4% (2.9%), while that of the RPSP scheme does not exceed 0.7% (0.6%) in UOX (MOX) slabs. At the same point, the overestimations of the G4- $[\gamma + \text{ann}]$  and S2-[TTB=0] schemes are 1.4% and 2.4%, respectively. Table V lists the average and maximum errors for each reactor compartment. We see that the average gain in accuracy guaranteed by the RPSP-based scheme is 4.6 and 3.1 times that for Liegeard's scheme in MOX and UOX slabs, respectively. The corresponding gain is 2 and 4.9 times that for Liegeard's scheme in the vessel and shielding of the reactor, respectively. For such isotropies, material types, densities, and energies, the assumptions A1–A3 of the TTB model hold well, and thus any exclusion of TTB induces considerable error everywhere.

#### IV. CONCLUSION

Fully coupled photon-electron-positron computational schemes are needed in a broad range of domains, from radiotherapy and radiosurgery treatment planning to nuclear-reactor safety analysis. For decades, the industrial deployment of such schemes has remained problematic because of the persisting time-consuming aspects of condensed-history algorithms and Boltzmann-Fokker-Planck solvers. Semiempirical models then took their place

as operational clinical algorithms, with well-known costly errors (approximately 20%) within heterogeneities. In this paper, a partially coupled scheme is introduced. Its multidisciplinary impact is quantified by comparison with state-of-the-art coupled and uncoupled schemes. The proposed scheme is based on the formal transport of neutral particles, while the long-range effects of charged particles are recovered by reactor-physics models for secondary photons. RPSPs include TTB, annihilation, and full atomic relaxation cascade models. Charged-particle transport is avoided by forcing (1) bremsstrahlung photons to inherit the incident particle's direction and birth point, and (2) isotropic emission of annihilation photons at the site of pair production.

Typical clinical beam spectra are analyzed for the Rogers and Mohan benchmark. Within tissues, the average error of the RPSP scheme from the fully coupled scheme is of the order of 0.5%. The maximum within-tissue discrepancies do not exceed 1.3% at high energies. High-atomic-number and dense materials, such as bone and prostheses, highlight the further impact of the RPSP-based scheme. The CPU time of a typical coupled scheme is reduced by 58 and 78 times for 3- and 6-MeV beams, respectively. The lack of electronic disequilibrium and backscattering models implies localized buildup and interface errors. These are the only significant discrepancies observed. A higher impact is observed for the irradiation of  ${}^4\text{Be}$ ,  ${}^6\text{C}$ ,  ${}^{13}\text{Al}$ ,  ${}^{26}\text{Fe}$ ,  ${}^{29}\text{Cu}$ ,  ${}^{32}\text{Ge}$ ,  ${}^{47}\text{Ag}$ ,  ${}^{79}\text{Au}$ ,  ${}^{82}\text{Pb}$ , and  ${}^{92}\text{U}$  slabs. In most of these cases, for all energies studied (in the interval [21 keV, 7 MeV]), the errors with respect to the fully coupled scheme are lower than 1% at the hottest point of the slab. At 7 MeV, the RPSPs reduce the overestimations at the hottest point in the current uncoupled scheme by 9–12 times in aluminum, copper, gold, and uranium. A 3D spatial analysis shows that the impact of the RPSPs is demarcated everywhere and increases with energy, atomic number, and material density. A jump in the RPSP error from 0.8% to 1.6% is observed for the lead slab between 5.75 and 6 MeV. This jump is due to the inability of the CSDA, included in the TTB model, to handle catastrophic collisions. The impact of RPSPs is also quantified for a multislab reactor benchmark. The mean errors with respect to the fully coupled scheme within the reactor shielding, vessel, and fuel are 0.1%, 0.4%, and 0.8%, respectively. The overestimation of the power peaking factor by the

state-of-the-art uncoupled scheme is reduced from 3.6 to 5.1 times for UOX and MOX slabs, respectively.

Further gains in accuracy for monodirectional beams are possible by revisiting TTB. Finally, the implementation of RPSPs in Boltzmann solvers could lead to computation times of industrial and clinical interest.

### ACKNOWLEDGMENTS

This work was supported by a Discovery Grant from the Natural Science and Engineering Research Council of Canada (NSERC), a grant from the Collaborative Research and Training Experience (CREATE-481695-2016) Program in Simulation-based Engineering Science (Génie Par la Simulation), and the Canada First Research Excellence Fund through the TransMedTech Institute.

- [1] J. Hubbell, *Radiation Physics, Encyclopedia of Physical Science and Technology* Vol. 3 (Academic Press, New York, USA, 2001), 3rd ed.
- [2] J. C. Garth, Electron/photon transport and its applications, *The Monte Carlo Method: Versatility Unbounded in a Dynamic Computing World*, Chattanooga, Tennessee, 172005.
- [3] J. Morel, Fokker-Planck calculations using standard discrete ordinates transport codes, *Nucl. Sci. Eng.* **79**, 340 (1981).
- [4] J. Morel, A synthetic acceleration method for discrete ordinates calculations with highly anisotropic scattering, *Nucl. Sci. Eng.* **82**, 34 (1982).
- [5] H. Hensel, R. Iza-Teran, and N. Siedow, Deterministic model for dose calculation in photon radiotherapy, *Phys. Med. Biol.* **51**, 675 (2006).
- [6] J. Caron, J.-L. Feugeas, B. Dubroca, G. Kantor, C. Dejean, G. Birindelli, T. Pichard, P. Nicolai, E. d'Humières, and M. Frank, *et al.*, Deterministic model for the transport of energetic particles: Application in the electron radiotherapy, *Phys. Med.* **31**, 912 (2015).
- [7] E. Olbrant and M. Frank, Generalized Fokker-Planck theory for electron and photon transport in biological tissues: Application to radiotherapy, *Comput. Math. Methods Med.* **11**, 313 (2010).
- [8] C. Zerby and F. Keller, Electron transport theory, calculations, and experiments, *Nucl. Sci. Eng.* **27**, 190 (1967).
- [9] D. E. Bartine, R. Alsmiller Jr, F. Mynatt, W. Engle Jr, and J. Barish, Low-energy electron transport by the method of discrete ordinates, *Nucl. Sci. Eng.* **48**, 159 (1972).
- [10] J. W. Wilson, F. F. Badavi, F. A. Cucinotta, J. L. Shinn, G. D. Badhwar, R. Silberberg, C. Tsao, L. W. Townsend, and R. K. Tripathi, *HZETRN: Description of a free-space ion and nucleon transport and shielding computer program*, Tech. Rep. (Tech. Rep. NASA TP-3495, National Aeronautics and Space Administration, 1995, 1995).
- [11] M. Stanford and J. A. Jones, Space radiation concerns for manned exploration, *Acta Astronaut.* **45**, 39 (1999).
- [12] I. G. Usoskin, L. Desorgher, P. Velinov, M. Storini, E. O. Flückiger, R. Bütikofer, and G. A. Kovaltsov, Ionization of the earth's atmosphere by solar and galactic cosmic rays, *Acta Geophys.* **57**, 88 (2009).
- [13] G. A. Nelson, Space radiation and human exposures, a primer, *Rad. Res.* **185**, 349 (2016).
- [14] F. Pleasonton, R. L. Ferguson, and H. Schmitt, Prompt gamma rays emitted in the thermal-neutron-induced fission of U-235, *Phys. Rev., C Nucl. Phys.* **6**, 1023 (1972).
- [15] V. Verbinski, H. Weber, and R. Sund, Prompt gamma rays from U 235 (n, f), Pu 239 (n, f), and spontaneous fission of Cf 252, *Phys. Rev., C Nucl. Phys.* **7**, 1173 (1973).
- [16] T. E. Valentine, Evaluation of prompt fission gamma rays for use in simulating nuclear safeguard measurements, *Ann. Nucl. Energy* **28**, 191 (2001).
- [17] A. Hébert, *Applied Reactor Physics* (Presses Internationales Polytechnique, Montreal, Canada, 2009), 3rd ed.
- [18] W. M. Stacey, *Nuclear Reactor Physics* (John Wiley & Sons, Atlanta, USA, 2018).
- [19] A. Hébert, A review of legacy and advanced self-shielding models for lattice calculations, *Nucl. Sci. Eng.* **155**, 310 (2007).
- [20] Z. Bilanovic and D. R. McCracken, Neutron-photon energy deposition in CANDU reactor fuel channels: A comparison of modelling techniques using anisn and MCNP computer codes. AECL Research No. AECL-111601994.
- [21] A. Mylonakis, M. Varvayanni, N. Catsaros, P. Savva, and D. Grigoriadis, Multi-physics and multi-scale methods used in nuclear reactor analysis, *Ann. Nucl. Energy* **72**, 104 (2014).
- [22] L. Lorence, J. Morel, and G. Valdez, Physics guide to CEPXS: A multigroup coupled electron-photon cross section generating code, SAND89-1685, Sandia National Laboratory 1989.
- [23] A. Voloschenko and V. Kryuchkov, *KATRIN-2.5, Three-dimensional discrete ordinates neutron, photon and charged particles transport code*, Tech. Rep. (Russian Academy of Sciences, KIAM No. 7-27-2004 (Rev, September 2009), 2009).
- [24] I. Kawrakow and A. F. Bielajew, On the condensed history technique for electron transport, *Nucl. Ins. Methods Phys. Res. Sect. B: Beam Interact. with Mater. At.* **142**, 253 (1998).
- [25] I. H. Bae, M. G. Na, Y. J. Lee, and G. C. Park, Calculation of the power peaking factor in a nuclear reactor using support vector regression models, *Ann. Nucl. Energy* **35**, 2200 (2008).
- [26] C. Liegeard, A. Calloo, G. Marleau, and E. Girardi, in *M&C 2017 - International Conference on Mathematics & Computational Methods Applied to Nuclear Science & Engineering*, April 16-20, Jeju, Korea (2017).
- [27] M. Hayns, The evolution of probabilistic risk assessment in the nuclear industry, *Process Saf. Environ. Prot.* **77**, 117 (1999).
- [28] S. Webb, *The Physics of Three Dimensional Radiation Therapy: Conformal Radiotherapy, Radiosurgery and Treatment Planning* (CRC Press, Sutton, UK, 1993).
- [29] A. Ahnesjö and M. M. Aspradakis, Dose calculations for external photon beams in radiotherapy, *Phys. Med. Biol.* **44**, R99 (1999).

- [30] M. Van Herk, in *Seminars in Radiation Oncology*, Vol. 14 (Elsevier, 2004), p. 52.
- [31] Prescribing, Recording, and Reporting Photon-Beam Intensity-Modulated Radiation Therapy (IMRT), J. Int. Commission Rad. Units Meas. **10**, NP2016.
- [32] B. A. Fraass, J. Smathers, and J. Deye, Summary and recommendations of a National Cancer Institute workshop on issues limiting the clinical use of Monte Carlo dose calculation algorithms for megavoltage external beam radiation therapy, *Med. Phys.* **30**, 3206 (2003).
- [33] J. Shafiq, M. Barton, D. Noble, C. Lemer, and L. J. Donaldson, An international review of patient safety measures in radiotherapy practice, *Radiother. Oncol.* **92**, 15 (2009).
- [34] N. Papanikolaou, J. J. Battista, A. L. Boyer, C. Kappas, E. Klein, T. R. Mackie, M. Sharpe, and J. Van Dyk, Tissue inhomogeneity corrections for megavoltage photon beams, AAPM Task Group **65**, 1 (2004).
- [35] T. Mackie, J. Scrimger, and J. Battista, A convolution method of calculating dose for 15-MV x rays, *Med. Phys.* **12**, 188 (1985).
- [36] R. Mohan, C. Chui, and L. Lidofsky, Differential pencil beam dose computation model for photons, *Med. Phys.* **13**, 64 (1986).
- [37] H. M. Kooy and H. Rashid, A three-dimensional electron pencil-beam algorithm, *Phys. Med. Biol.* **34**, 229 (1989).
- [38] A. Ahnesjö, M. Saxner, and A. Trepp, A pencil beam model for photon dose calculation, *Med. Phys.* **19**, 263 (1992).
- [39] A. Ahnesjö, Collapsed cone convolution of radiant energy for photon dose calculation in heterogeneous media, *Med. Phys.* **16**, 577 (1989).
- [40] A. Boyer and E. Mok, A photon dose distribution model employing convolution calculations, *Med. Phys.* **12**, 169 (1985).
- [41] M. M. Aspradakis, R. H. Morrison, N. D. Richmond, and A. Steele, Experimental verification of convolution/superposition photon dose calculations for radiotherapy treatment planning, *Phys. Med. Biol.* **48**, 2873 (2003).
- [42] K. R. Hogstrom, M. D. Mills, and P. R. Almond, Electron beam dose calculations, *Phys. Med. Biol.* **26**, 445 (1981).
- [43] E. Fermi, The ionization loss of energy in gases and in condensed materials, *Phys. Rev.* **57**, 485 (1940).
- [44] L. Eyges, Multiple scattering with energy loss, *Phys. Rev.* **74**, 1534 (1948).
- [45] T. Knoos, A. Ahnesjö, P. Nilsson, and L. Weber, Limitations of a pencil beam approach to photon dose calculations in lung tissue, *Phys. Med. Biol.* **40**, 1411 (1995).
- [46] W. Ulmer, J. Pyry, and W. Kaissl, A 3D photon superposition/convolution algorithm and its foundation on results of Monte Carlo calculations, *Phys. Med. Biol.* **50**, 1767 (2005).
- [47] L. Tillikainen, H. Helminen, T. Torsti, S. Siljamäki, J. Alakuijala, J. Pyry, and W. Ulmer, A 3D pencil-beam-based superposition algorithm for photon dose calculation in heterogeneous media, *Phys. Med. Biol.* **53**, 3821 (2008).
- [48] L. R. Aarup, A. E. Nahum, C. Zacharou, T. Juhler-Nøttrup, T. Knöös, H. Nyström, L. Specht, E. Wieslander, and S. S. Korreman, The effect of different lung densities on the accuracy of various radiotherapy dose calculation methods: Implications for tumour coverage, *Radiother. Oncol.* **91**, 405 (2009).
- [49] T. Krieger and O. A. Sauer, Monte Carlo-versus pencil-beam/collapsed-cone-dose calculation in a heterogeneous multi-layer phantom, *Phys. Med. Biol.* **50**, 859 (2005).
- [50] S. A. Enger, J. Vijande, and M. J. Rivard, in *Seminars in Radiation Oncology*, Vol. 30 (Elsevier, 2020), p. 77.
- [51] M. J. Berger and R. Wang, in *Monte Carlo Transport of Electrons and Photons* (Springer, 1988), p. 21.
- [52] M. M. Savatos, in *Joint International Conference on Mathematical Methods and Supercomputing for Nuclear Applicationsn, October 6-10. New York, USA.* (Lawrence Livermore National Laboratory, 1997), p. 1.
- [53] C. R. Drumm, W. C. Fan, L. Lorence, and J. Liscum-Powell, An analysis of the extended-transport correction with application to electron beam transport, *Nucl. Sci. Eng.* **155**, 355 (2007).
- [54] G. Pomraning, Higher order Fokker-Planck operators, *Nucl. Sci. Eng.* **124**, 390 (1996).
- [55] C. L. Leakeas and E. W. Larsen, Generalized Fokker-Planck approximations of particle transport with highly forward-peaked scattering, *Nucl. Sci. Eng.* **137**, 236 (2001).
- [56] D. E. Pelowitz, *MCNP- A General Monte Carlo N-Particle Transport Code, Version 5, User's Guide*, Tech. Rep. (Los Alamos National Laboratory, LA-CP-03-0245 (Rev.1, January 2008), 2008).
- [57] J. Halbleib, in *Monte Carlo Transport of Electrons and Photons* (Springer, 1988), p. 249.
- [58] S. Agostinelli, J. Allison, K. a. Amako, J. Apostolakis, H. Araujo, P. Arce, M. Asai, D. Axen, S. Banerjee, and G. Barrand, *et al.*, GEANT4—a simulation toolkit, *Nuclear Instruments and Methods in Physics Research Section A: Accelerators, Spectrom., Detectors and Associated Equipment* **506**, 250 (2003).
- [59] F. Salvat, in *Workshop proceedings OECD, Barcelona, Spain. Jan. 28 - Feb. 1* (Nuclear Energy Agency, 2019), p. 1.
- [60] T. Sato, Y. Iwamoto, S. Hashimoto, T. Ogawa, T. Furuta, S.-i. Abe, T. Kai, P.-E. Tsai, N. Matsuda, and H. Iwase, *et al.*, Features of particle and heavy ion transport code system (PHITS) version 3.02, *J. Nucl. Sci. Technol.* **55**, 684 (2018).
- [61] C. Ahdida, D. Bozzato, D. Calzolari, F. Cerutti, N. Charitonidis, A. Cimmino, A. Coronetti, G. D'Alessandro, A. Donadon Servelle, and L. Esposito, *et al.*, New capabilities of the FLUKA multi-purpose code, *Front. Phys.*, 7052022.
- [62] N. V. Mokhov and C. C. James, *The MARS code system user's guide version 15 (2016)*, Tech. Rep. (Fermi National Accelerator Lab.(FNAL), Batavia, IL (United States), 2017).
- [63] I. Kawrakow, D. Rogers, E. Mainegra-Hing, F. Tessier, R. Townson, and B. Walters, EGSnrc toolkit for Monte Carlo simulation of ionizing radiation transport, doi **10**, 400013032000.
- [64] T. Kaltiaisenaho, *Implementing a photon physics model in Serpent-2*, Ph.D. thesis, Aalto University School of Science (2016).

- [65] A. Lund and P. Romano, *Implementation and Validation of Photon Transport in OpenMC*, Tech. Rep. (Argonne National Laboratory, ANL/MCS-TM-381, 2018).
- [66] J. Leppänen, M. Pusa, T. Viitanen, V. Valtavirta, and T. Kaltiaisenaho, The Serpent Monte Carlo code: Status, development and applications in 2013, *Ann. Nucl. Energy* **82**, 142 (2015).
- [67] J. Leppänen, Performance of Woodcock delta-tracking in lattice physics applications using the Serpent Monte Carlo reactor physics burnup calculation code, *Ann. Nucl. Energy* **37**, 715 (2010).
- [68] J. Leppänen, A new assembly-level Monte Carlo neutron transport code for reactor physics calculations, *Mathematics and Computation, Supercomputing, Reactor Physics and Nuclear and Biological Applications*. Palais des Papes, Avignon, France, September, 12-15, 1 (2005).
- [69] J. Leppänen, *Development of a new Monte Carlo reactor physics code*, Ph.D. thesis, Helsinki University of Technology (2007).
- [70] E. Fridman and J. Leppänen, On the use of the Serpent Monte Carlo code for few-group cross section generation, *Ann. Nucl. Energy* **38**, 1399 (2011).
- [71] J. Leppänen, M. Pusa, and E. Fridman, Overview of methodology for spatial homogenization in the Serpent 2 Monte Carlo code, *Ann. Nucl. Energy* **96**, 126 (2016).
- [72] M. Aufiero, A. Cammi, C. Fiorina, J. Leppänen, L. Luzzi, and M. E. Ricotti, An extended version of the Serpent-2 code to investigate fuel burn-up and core material evolution of the molten salt fast reactor, *J. Nucl. Mater.* **441**, 473 (2013).
- [73] J. Leppänen, T. Viitanen, and V. Valtavirta, Multi-physics coupling scheme in the Serpent 2 Monte Carlo code, *Trans. Am. Nucl. Soc.* **107**, 1165 (2012).
- [74] J. Leppänen, Modeling of nonuniform density distributions in the Serpent 2 Monte Carlo code, *Nucl. Sci. Eng.* **174**, 318 (2013).
- [75] J. Leppänen, V. Hovi, T. Ikonen, J. Kurki, M. Pusa, V. Valtavirta, and T. Viitanen, The numerical multi-physics project (NUMPS) at VTT Technical Research Centre of Finland, *Ann. Nucl. Energy* **84**, 55 (2015).
- [76] J. Leppänen and T. Kaltiaisenaho, in *International Conference on the Physics of Reactors, PHYSOR 2016: Unifying Theory and Experiments in the 21st Century, May 1-5, Sun Valley, USA*. (American Nuclear Society (ANS), 2016).
- [77] J. Leppänen, T. Kaltiaisenaho, V. Valtavirta, and M. Metsälä, in *International Conference on Mathematics and Computational Methods Applied to Nuclear Science and Engineering, M&C 2017, Jeju, Korea, April 16-20*. (2017).
- [78] T. Kaltiaisenaho, *Implementing a beta bremsstrahlung source in Serpent*, Tech. Rep. (VTT-R-00953-18, VTT Technical Research Centre of Finland Ltd., 2018).
- [79] R. Tuominen, V. Valtavirta, and J. Leppänen, New energy deposition treatment in the Serpent 2 Monte Carlo transport code, *Ann. Nucl. Energy* **129**, 224 (2019).
- [80] V. Vlachoudis, in *M&C 2017 - International Conference on Mathematics, Computational Methods & Reactor Physics, May 3-7, Saratoga Springs, New York, USA* (2009).
- [81] R. Collaboration, Geant4: An object-oriented toolkit for simulation in HEP, CERN Report CERN/LHCC 98 44, 1998.
- [82] J. Allison, K. Amako, J. Apostolakis, H. Araujo, P. A. Dubois, M. Asai, G. Barrand, R. Capra, S. Chauvie, and R. Chytracsek, *et al.*, Geant4 developments and applications, *IEEE Trans. Nucl. Sci.* **53**, 270 (2006).
- [83] A. Ribon, J. Apostolakis, A. Dotti, G. Folger, V. Ivanchenko, M. Kosov, V. Uzhinsky, and D. Wright, Status of Geant4 hadronic physics for the simulation of LHC experiments at the start of LHC physics program, *CERN-LCGAPP* **2**, 2010 (2010).
- [84] E. Daly, H. Evans, F. Lei, F. Longo, S. Magni, R. Nartallo, P. Nieminen, M. Pia, and P. Truscott, in *Advanced Monte Carlo for Radiation Physics, Particle Transport Simulation and Applications* (Springer, 2001), p. 401.
- [85] M. Asai, R. A. Reed, and R. A. Weller, in *Astroparticle, Particle And Space Physics, Detectors And Medical Physics Applications* (World Scientific, 2006), p. 429.
- [86] J.-F. Carrier, L. Archambault, L. Beaulieu, and R. Roy, Validation of Geant4, an object-oriented Monte Carlo toolkit, for simulations in medical physics, *Med. Phys.* **31**, 484 (2004).
- [87] E. Poon and F. Verhaegen, Accuracy of the photon and electron physics in Geant4 for radiotherapy applications, *Med. Phys.* **32**, 1696 (2005).
- [88] J. Spiga, E. Siegbahn, E. Bräuer-Krisch, P. Randaccio, and A. Bravin, The Geant4 toolkit for microdosimetry calculations: Application to microbeam radiation therapy (MRT), *Med. Phys.* **34**, 4322 (2007).
- [89] S. Chauvie, Z. Francis, S. Guatelli, S. Incerti, B. Mascialino, P. Moretto, P. Nieminen, and M. G. Pia, Geant4 physics processes for microdosimetry simulation: Design foundation and implementation of the first set of models, *IEEE Trans. Nucl. Sci.* **54**, 2619 (2007).
- [90] I. Kyriakou, D. Emfietzoglou, V. Ivanchenko, M. Borge, S. Guatelli, P. Lazarakis, H. Tran, and S. Incerti, Microdosimetry of electrons in liquid water using the low-energy models of Geant4, *J. Appl. Phys.* **122**, 024303 (2017).
- [91] C. Villagrasa, Z. Francis, and S. Incerti, Physical models implemented in the GEANT4-DNA extension of the GEANT-4 toolkit for calculating initial radiation damage at the molecular level, *Radiat. Prot. Dosimetry* **143**, 214 (2011).
- [92] S. Incerti, G. Baldacchino, M. Bernal, R. Capra, C. Champion, Z. Francis, P. Gueye, A. Mantero, B. Mascialino, and P. Moretto, *et al.*, The Geant4-DNA project, *Int. J. Model., Simul., Sci. Comput.* **1**, 157 (2010).
- [93] S. Pistrui-Maximean, N. Freud, J. Létang, A. Koch, B. Munier, A. Walenta, G. Montarou, and D. Babot, Geant4 simulation of the response of phosphor screens for X-ray imaging, *Nucl. Instrum. Methods Phys. Res. Sect. A: Accel., Spectrom., Detect. Associated Equip.* **563**, 196 (2006).
- [94] T. Kaltiaisenaho, Photon transport physics in Serpent 2 Monte Carlo code, *Comput. Phys. Commun.* **252**, 107143 (2020).



- [95] D. Cullen, *A Survey of Photon Cross Section Data for Use in EPICS2017*, Tech. Rep. (Nuclear Data Services, IAEA-NDS-225 (Rev.1, February 2018), 2018).
- [96] D. Cullen, *A Survey of Electron Cross Section Data for Use in EPICS2017*, Tech. Rep. (Nuclear Data Services, IAEA-NDS-226 (December 2017), 2017).
- [97] D. Cullen, *A Survey of Atomic Binding Energies for Use in EPICS2017*, Tech. Rep. (Nuclear Data Services, IAEA-NDS-224 (Rev.1, April 2018), 2018).
- [98] Geant-4 Collaboration, *Physics Reference Manual-Release 10.6*, Tech. Rep. (CERN, Geneva, Rev4.0: December 6th, 2019., 2019).
- [99] M. Berger, J. Coursey, and Zucker, ESTAR, PSTAR, and ASTAR: Computer programs for calculating stopping-power and range tables for electrons, protons, and helium ions (version 1.21) (1999), <http://physics.nist.gov/Star>.
- [100] R. Sternheimer, S. Seltzer, and M. Berger, Density effect for the ionization loss of charged particles in various substances, *Phys. Rev. B* **26**, 6067 (1982).
- [101] H. Bethe, Bremsformel für elektronen relativistischer geschwindigkeit, *Z. für Phys.* **76**, 293 (1932).
- [102] L. Kim, R. Pratt, S. Seltzer, and M. Berger, Ratio of positron to electron bremsstrahlung energy loss: An approximate scaling law, *Phys. Rev. A* **33**, 3002 (1986).
- [103] W. Heitler, *The Quantum Theory of Radiation* (Oxford Clarendon Press, Oxford, UK, 1984).
- [104] F. Salvat and J. M. Fernández-Varea, Overview of physical interaction models for photon and electron transport used in Monte Carlo codes, *Metrologia* **46**, S112 (2009).
- [105] G. Roach, J. Tickner, and Y. V. Haarlem, Discrepancies in atomic shell and fluorescent x-ray energies in the evaluated photon data library EPDL97, *Xray Spectrom.* **41**, 279 (2012).
- [106] M. Augelli, S. Hauf, M. Kuster, M. Han, C. Kim, M. Pia, L. Quintieri, H. Seo, P. Saracco, and G. Weidenspointner, *et al.*, in *IEEE Nuclear Science Symposium & Medical Imaging Conference* (IEEE, 2010), p. 307.
- [107] M. G. Pia, H. Seo, M. Batic, M. Begalli, C. H. Kim, L. Quintieri, and P. Saracco, Evaluation of atomic electron binding energies for Monte Carlo particle transport, *IEEE Trans. Nucl. Sci.* **58**, 3246 (2011).
- [108] S. Perkins, D. Cullen, M. Chen, J. Hubbel, J. Rathkopf, and J. Scofield, *Tables and Graphs of Atomic Subshell and Relaxation Data Derived from the LLNL Evaluated Atomic Data Library (EADL), Z=1-100*, Tech. Rep. (Lawrence Livermore National Lab., UCRL-50400 Vol 30 DE92 007985, 1991).
- [109] D. Cullen, *EPICS-2017: April 2019 Status Report*, Tech. Rep. (Nuclear Data Services, IAEA-NDS-228, 2019).
- [110] D. Rogers and R. Mohan, in *The Use of Computers in Radiation Therapy* (Springer, 2000), p. 120.
- [111] S. García-Pareja, A. M. Lallena, and F. Salvat, Variance-reduction methods for Monte Carlo simulation of radiation transport, *Front. Phys.*, 6332021.
- [112] J. Sempau, A. Badal, and L. Brualla, A Penelope-based system for the automated Monte Carlo simulation of clinacs and voxelized geometries—application to far-from-axis fields, *Med. Phys.* **38**, 5887 (2011).
- [113] J. P. Archambault and E. Mainegra-Hing, Comparison between EGSnrc, Geant4, MCNP5 and Penelope for mono-energetic electron beams, *Phys. Med. Biol.* **60**, 4951 (2015).
- [114] M. Vilches, S. Garcia-Pareja, R. Guerrero, M. Anguiano, and A. Lallena, Monte Carlo simulation of the electron transport through air slabs: A comparative study of Penelope, Geant3, Geant4 and EGSnrc Monte Carlo codes, *IEEE Trans. Nucl. Sci.* **55**, 710 (2008).
- [115] E. Poon, J. Seuntjens, and F. Verhaegen, Consistency test of the electron transport algorithm in the Geant4 Monte Carlo code, *Phys. Med. Biol.* **50**, 681 (2005).
- [116] H. B. Abdelouahed, S. Incerti, and A. Mantero, New Geant4 cross section models for PIXE simulation, *Nucl. Instrum. Methods Phys. Res. Sect. B: Beam Interact. Mater. At.* **267**, 37 (2009).
- [117] G. Marleau, A. Hébert, and R. Roy, A User Guide for DRAGON Version 5, Institut de génie nucléaire, Département de génie physique, École Polytechnique de Montréal. Montréal, QC, Canada, Tech. Rep. IGE-335 (2021).
- [118] T. Goorley, M. James, T. Booth, F. Brown, J. Bull, L. Cox, J. Durkee, J. Elson, M. Fensin, and R. Forster, *et al.*, Initial MCNP6 release overview, *Nucl. Technol.* **180**, 298 (2012).